PERGAMON

International Journal of Heat and Mass Transfer 44 (2001) 3053–3065

International Journal of HEAT and MASS TRANSFER

www.elsevier.com/locate/ijhmt

Low-Prandtl number natural convection in volumetrically heated rectangular enclosures III. Shallow cavity, AR = 0.25

Salvatore Arcidiacono, Michele Ciofalo *

Dipartimento di Ingegneria Nucleare, Università di Palermo, Viale delle Scienze, 90128 Palermo, Italy

Received 30 May 2000; received in revised form 29 October 2000

Abstract

Following previous studies for enclosures of aspect ratios 4 and 1, direct numerical two-dimensional simulations were conducted for the free convection flow of a low-Prandtl number fluid with internal heat generation in a shallow cavity (AR = 0.25) having adiabatic top and bottom walls and isothermal side walls. The Prandtl number was 0.0321 and the Grashof number, *Gr*, based on power density and cavity width, ranged from 10^6 to 10^{11}. The flow was steady for *Gr* up to 3×10^9, time-periodic for $Gr \approx 10^{10}$ and chaotic for $Gr \geqslant 3 \times 10^{10}$. In both the steady and the periodic regimes, the flow was instantaneously symmetric with respect to the vertical centreline of the enclosure; in the chaotic regime the instantaneous flow was asymmetric, but bilateral symmetry was recovered in the time-averaged velocity and temperature fields. For Grashof numbers above $\sim 10^7$, the Nusselt number (overall/conductive heat transfer) increased roughly as $Gr^{1/5}$, i.e., slightly more markedly than for the previous aspect ratios and in agreement with the behaviour expected in the separated-boundary layer regime.

1. Introduction and previous work

Free convection in enclosures with internal heat generation is encountered in a variety of fields, ranging from the geophysics of the Earth's mantle to the cooling of a molten nuclear reactor core [1]. Therefore, a considerable research effort, both experimental and computational, has been dedicated to the phenomenon [2–5]. However, the problem is characterized by a considerable number of variables, including the Prandtl and Grashof numbers, the shape of the enclosure, and the thermal boundary conditions, so that a large number of basic configurations can be identified, each exhibiting a peculiar behaviour. Only a very small portion of this configuration space has been studied so far; in particular, for the case of low-Prandtl number fluids in side-cooled enclosures, the only available results are analytical (linear theory) predictions of the loss of stability of the base parallel flow in infinitely slender two-dimensional slots, obtained over forty years ago by Gershuni and co-workers and reported in their review by Kulacki and Richards [1].

Therefore, a research programme was initiated with the purpose of predicting flow regimes and basic heat transfer phenomena, and of testing the applicability of conventional turbulence models, for side-cooled, internally heated enclosures at low *Pr*, using direct two-dimensional numerical simulations. The study was initially suggested by the cooling problems encountered in liquid metal breeder blankets for nuclear fusion power reactors; in particular, the Prandtl number chosen ($Pr = 0.0321$) corresponds to a liquid metal Li–17Pb alloy at ~300°C, of particular interest in the DEMO-WCLL blanket design [6]. However, the results proved to be of intrinsic interest as basic fluid dynamics.

In papers [7,8], direct numerical two-dimensional simulations are reported for aspect ratios (height/width) 4 and 1, respectively. The Grashof number, based on the maximum conductive temperature and on the cavity *width*, ranged from $\sim 10^4$ to $\sim 10^9$. According to the values of AR and *Gr*, different regimes were predicted, including steady-state, periodic, and chaotic flows.

* Corresponding author. Tel.: +39-91-232257, fax: +39-91-232215.

E-mail address: ciofalo@din.din.unipa.it (M. Ciofalo).

0017-9310/01/$ - see front matter
PII: S0017-9310(00)00347-1

Nomenclature

AR	cavity aspect ratio, height/width (dimensionless)
D	cavity width (m)
e	turbulence energy normalized by U_0^2 (dimensionless)
F	frequency (s^{-1})
f	frequency normalized by $1/\tau_0$ (dimensionless)
g	acceleration due to gravity (m s^{-2})
Gr	Grashof number, $g\beta qD^5/(kv^2) = Ra/Pr$ (dimensionless)
Gr_H	Grashof number based on H, $AR^3 Gr$ (dimensionless)
k	thermal conductivity (W m^{-1} K^{-1})
Nu_1	first Nusselt number, $1/T_{max}$ (dimensionless)
Nu_2	second Nusselt number, $(2/3)/\langle T\rangle$ (dimensionless)
P	pressure (Pa)
p	pressure normalized by (ρU_0^2) (dimensionless)
Pr	Prandtl number, v/α (dimensionless)
q	power density (W m^{-3})
q''	heat flux (W m^{-2})
Ra	Rayleigh number, $Gr \times Pr$ (dimensionless)
S_w	wall shear stress normalized by $\mu U_0/D$ (dimensionless)
t	time normalized by τ_0 (dimensionless)
T	temperature normalized by ϑ_c (dimensionless)
U, V	velocity components (m s^{-1})
U_0	velocity scale, D/τ_0 (m s^{-1})
u, v	velocity components normalized by U_0 (dimensionless)
X, Y	coordinates (m)
x, y	coordinates normalized by D (dimensionless)

Greek symbols

α	thermal diffusivity (m^2 s^{-1})
β	thermal expansion coefficient (K^{-1})
ϑ	temperature (K)
ϑ_c	conductive temperature scale, $qD^2/8k$ (K)
μ	viscosity (N s m^{-2})
v	kinematic viscosity (m^2 s^{-1})
ρ	density (kg m^{-3})
τ	time (s)
τ_0	convective time scale, $(4\pi\sqrt{2}Gr^{-1/2})\tau_M$ (s)
τ_M	momentum diffusive time scale, D^2/v (s)
Ψ	stream function normalized by DU_0 (dimensionless)

Subscripts

BV	Brunt–Väisälä
c	conductive
max	maximum
P	periodic
w	wall
0	reference

For the *slender* enclosure (AR = 4), steady-state flow exhibiting bilateral (left–right) symmetry was predicted for Grashof numbers up to $\sim 2 \times 10^5$, chaotic flow for $Gr > \sim 10^6$, and periodic flow in a narrow intermediate range. The time-dependent flow field consisted of a central sinuous rising plume and of convection rolls, generated in the upper corners of the cavity and descending along the vertical isothermal walls. Up to the highest Grashof numbers studied the fluid motion exhibited a recognizable dominating frequency, associated with the process of roll renewal and scaling as $Gr^{1/2}$.

For the *square* enclosure (AR = 1), up to $Gr \approx 10^7$ the flow was steady and exhibited left–right symmetry. For $Gr \approx 3 \times 10^7$ symmetry was broken and asymmetric steady-state flow patterns were obtained. For $Gr \approx 5 \times 10^7$ the asymmetric flow became time-periodic. Finally, for $Gr \geqslant 10^8$, chaotic flow was predicted; the time-averaged velocity and temperature fields were still markedly asymmetric at $Gr = 10^8$, but re-attained bilateral symmetry at higher Gr (10^9), when developed two-dimensional turbulence was observed.

In the present paper, the study is extended to the case of a *shallow* enclosure (AR = 0.25) with the same thermal boundary conditions (side cooling). The Grashof number is made to vary in the range 10^6 to 10^{11} in order to observe the full range of flow regimes. The computational domain and the relevant nomenclature are shown in Fig. 1, where also the location of five monitoring points (referred to in the following) is indicated. The present study completes our investigation of internally heated, side-cooled enclosures at low Pr and, hopefully, contributes to fill a gap in the existing knowledge of confined free convection phenomena.

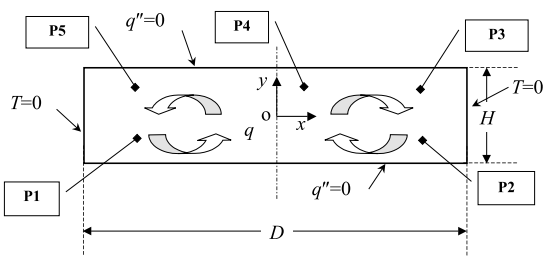

Fig. 1. Sketch of the model cavity of aspect ratio 0.25 with isothermal vertical walls and adiabatic horizontal walls. The location of monitoring points $P1$–$P5$ is indicated.

2. Model and numerical methods

With reference to the model problem sketched in Fig. 1, appropriate scales were chosen for length, temperature, time, velocity and pressure in order to write the governing equations in dimensionless form; the same approach as in [7,8] was followed. Thus, the length scale is the width D of the enclosure, while the temperature scale is the conductive peak temperature $\vartheta_c = qD^2/(8k)$. As regards the frequency or time scales, by analogy with the Brunt–Väisälä frequency $F_{BV} = (g\beta|\partial\vartheta/\partial Y|)^{1/2}/(2\pi)$ which characterizes stably stratified flows [9], the reference frequency $F_0 = (g\beta\vartheta_c/D)^{1/2}/(2\pi)$ was used. The corresponding time scale is $\tau_0 = F_0^{-1}$, which may be written as $\tau_0 = (4\pi\sqrt{2}Gr^{-1/2})\tau_M$, $\tau_M = D^2/\nu$ being the momentum diffusive time scale and $Gr = g\beta qD^5/(k\nu^2) = Ra/Pr$ the Grashof number. A velocity scale coherent with the above definitions is $U_0 = D/\tau_0$, i.e., the ratio of length to time scales. Finally, an appropriate pressure scale is ρU_0^2. As confirmed a posteriori by the computational results, the above choice of scales allowed all variables to remain of unity order throughout the range of parameters investigated.

The two-dimensional continuity and momentum equations, coupled with the energy transport equation under the Boussinesq approximation, may now be written in dimensionless form as:

$$\frac{\partial u}{\partial x} + \frac{\partial v}{\partial y} = 0, \tag{1}$$

$$\frac{\partial u}{\partial t} + u\frac{\partial u}{\partial x} + v\frac{\partial u}{\partial y} = -\frac{\partial p}{\partial x} + \frac{4\pi\sqrt{2}}{\sqrt{Gr}}\left(\frac{\partial^2 u}{\partial x^2} + \frac{\partial^2 u}{\partial y^2}\right), \tag{2a}$$

$$\frac{\partial v}{\partial t} + u\frac{\partial v}{\partial x} + v\frac{\partial v}{\partial y} = -\frac{\partial p}{\partial y} + \frac{4\pi\sqrt{2}}{\sqrt{Gr}}\left(\frac{\partial^2 v}{\partial x^2} + \frac{\partial^2 v}{\partial y^2}\right) + 4\pi^2 T, \tag{2b}$$

$$\frac{\partial T}{\partial t} + u\frac{\partial T}{\partial x} + v\frac{\partial T}{\partial y} = \frac{4\pi\sqrt{2}}{\sqrt{GrPr}}\left(\frac{\partial^2 T}{\partial x^2} + \frac{\partial^2 T}{\partial y^2} + 8\right), \tag{3}$$

in which $x = X/D$, $y = Y/D$, $u = U/U_0$, $v = V/U_0$, $p = P/(\rho U_0^2)$, $T = (\vartheta - \vartheta_w)/\vartheta_c$, $t = \tau/\tau_0$. The boundary conditions are:

$$u = v = 0, \quad \partial T/\partial y = 0 \text{ for } y = \pm AR/2 = \pm 1/8, \tag{4}$$

$$u = v = 0, \quad T = 0 \text{ for } x = \pm 1/2. \tag{5}$$

The range of Grashof numbers investigated was from 10^6 to 10^{11}. For $Gr < 10^6$, convection plays a negligible role in the present shallow geometry, while for $Gr > 10^{11}$ the explicit resolution of all energy-containing spatial and temporal features of the flow would require prohibitive computational grids and computing times.

Eqs. (1)–(3) were solved by using a finite-volume technique based on the SIMPLEC pressure–velocity coupling algorithm [10], Crank–Nicholson time stepping and the central discretization scheme both for the diffusion and for the advection terms. Details are given in [1]. The AEA code CFX4 [11] was used and simulations were run on a Pentium-III PC.

As will be discussed in the following sections, according to the Grashof number the flow either attained a steady-state configuration or exhibited periodic or chaotic unsteadiness. In the former case ($Gr \leqslant 3 \times 10^9$) the simulation was protracted until no significant variation of monitored quantities was observed. This required at most $\sim$10 time constants τ_0 (defined above), the dimensionless settling time increasing with the Grashof number. In all cases with time-dependent behaviour, the flow exhibited recognizable lowest frequencies ranging from $\sim 1.4/\tau_0$ (periodic flow obtained at $Gr = 10^{10}$) to $\sim 0.2/\tau_0$ (chaotic flow at $Gr = 3 \times 10^{10}$ and 10^{11}). Simulations were protracted in these cases for a dimensionless time of $\sim$40 to 60, so as to include (following the initial transient) several of the corresponding periods. One time unit τ_0 was resolved by 200 time steps; preliminary tests showed that increasing the temporal resolution above this value did not change the results to any appreciable extent.

Specific grid-independence tests were conducted for the present geometry; typical results are reported for the highest Gr studied (10^{11}) in Fig. 2. In graph (a), the dimensionless maximum and spatially averaged temperatures are plotted as functions of N_x (number of grid points along x), including results for five grids ranging from 40×20 to 160×80 ($x \times y$) nodes. In all cases, the number of grid points along y was $N_y = N_x/2$. Since the flow was time dependent (and chaotic) at this Gr, both T_{max} and $\langle T \rangle$ were time averaged over an adequately long simulation time ($t \approx 38$ to 58, see Section 5). Graph (b) reports a similar comparison for the maximum and spatially averaged dimensionless turbulence energy e, also computed over $\sim$20 time units. The results show that 128×64 nodes ensure a satisfactory grid independence not only of time-mean quantities but also of second-order statistics, such as the turbulence energy. The sensitivity to the number of grid points is even less at lower Grashof numbers.

The results presented in the following (encompassing steady, periodic and chaotic behaviours) were based on computational grids including 80×40 ($x \times y$) nodes for all steady-state cases at $Gr < 10^9$, 120×60 nodes for the steady-state case at $Gr = 10^9$, and 160×80 nodes for the time-dependent cases at higher Gr. The grids were selectively refined near the walls by using a hyperbolic tangent distribution.

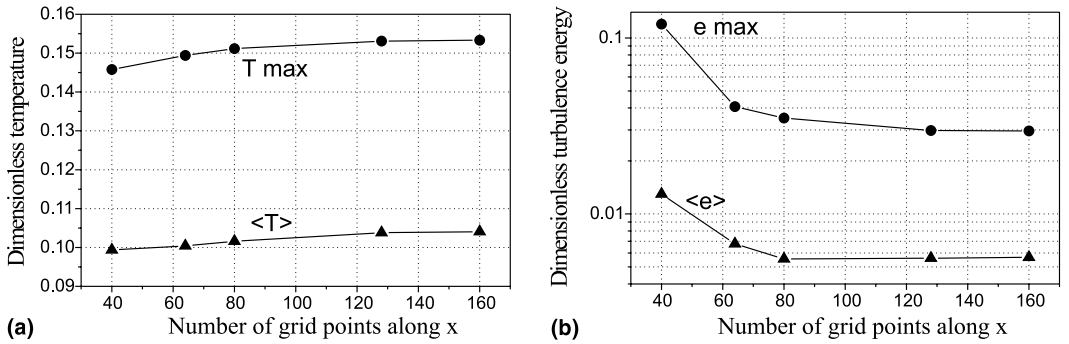

Fig. 2. Grid-independence assessment: time-averaged maximum and mean temperatures (a) and maximum and mean turbulence energies (b) in the enclosure for $Gr = 10^{11}$ and five computational grids of increasing density with $N_x = 2N_y$.

3. Steady-state flow

For $Gr \leqslant 3 \times 10^9$, the flow settled to a steady-state solution possessing bilateral symmetry. Fig. 3 reports mean (a) and maximum (b) temperatures as functions of time for $Gr = 10^6$ to 3×10^9. The initial temperature rate of rise in the cavity is the same at all points, and is given, in dimensionless terms, by $\partial T/\partial t = 32\pi\sqrt{2}/(Pr\sqrt{Gr})$ – as can be derived from Eq. (3) for initially negligible convection and diffusion – so that, in the dimensionless form used here, its slope decreases as Gr increases. At steady state, the maximum temperature is largest for $Gr = 10^6$, where the conductive unity value is recovered almost exactly due to the weak influence of convection on heat transfer. Because of the shallow shape of the enclosure, no vertical stratification is present in the region around the centreline, and hot fluid is not accumulated on the top of the cavity as observed for the former cases of AR = 1 and 4 [7,8], so that T_{max} never exceeds 1. As expected, mean temperatures in Fig. 3(a) decrease monotonically with Gr and are ~35% of the purely conductive value of 2/3 at $Gr = 10^9$.

Fig. 4 shows flow and temperature fields for the five steady-state cases investigated. It can be observed from the streamlines in graph (a) that the circulation cells become more round and obliquely oriented as the Grashof number increases. In the temperature fields (b), the increasing influence of convection with increasing Gr is made evident by the deformation of the isotherms. This results in a significant vertical thermal stratification, especially in the region between the centreline and the wall ($x \cong 0.25$), for the higher values of Gr.

Fig. 5(a) reports profiles of the (dimensionless) vertical velocity v as a function of the horizontal coordinate x along the midline $y = 0$ of the enclosure for all the steady-state cases studied. At the lowest Grashof number (10^6) the v profile is flat throughout the central region $-0.25 < x < 0.25$. For $Gr = 10^7$, a shallow central minimum appears in the v profile, while two upwelling hot plumes, in which v attains maxima of ~0.7, are formed around the locations $x = \pm 0.21$. As Gr increases further, v profiles become increasingly complex. A small central relative maximum appears around $x = 0$; the maximum positive v velocity attains a highest value of

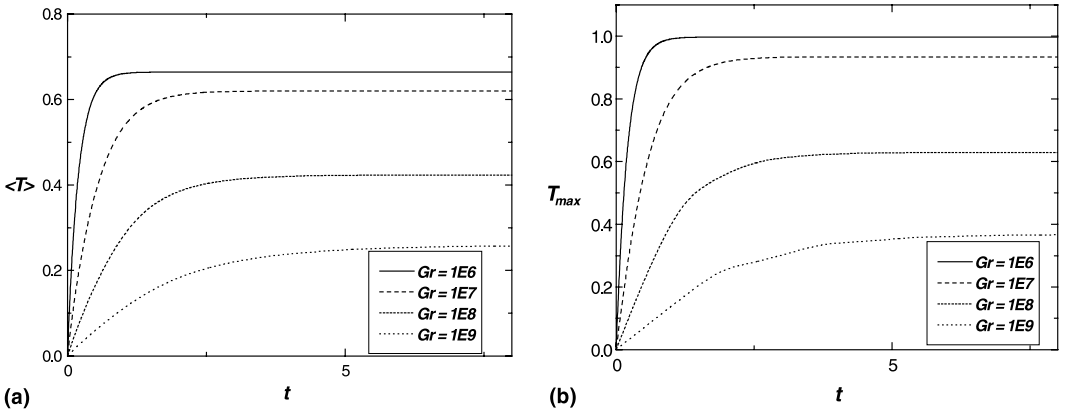

Fig. 3. Dimensionless mean (a) and maximum (b) temperatures as functions of time for four cases attaining symmetric steady-state conditions.

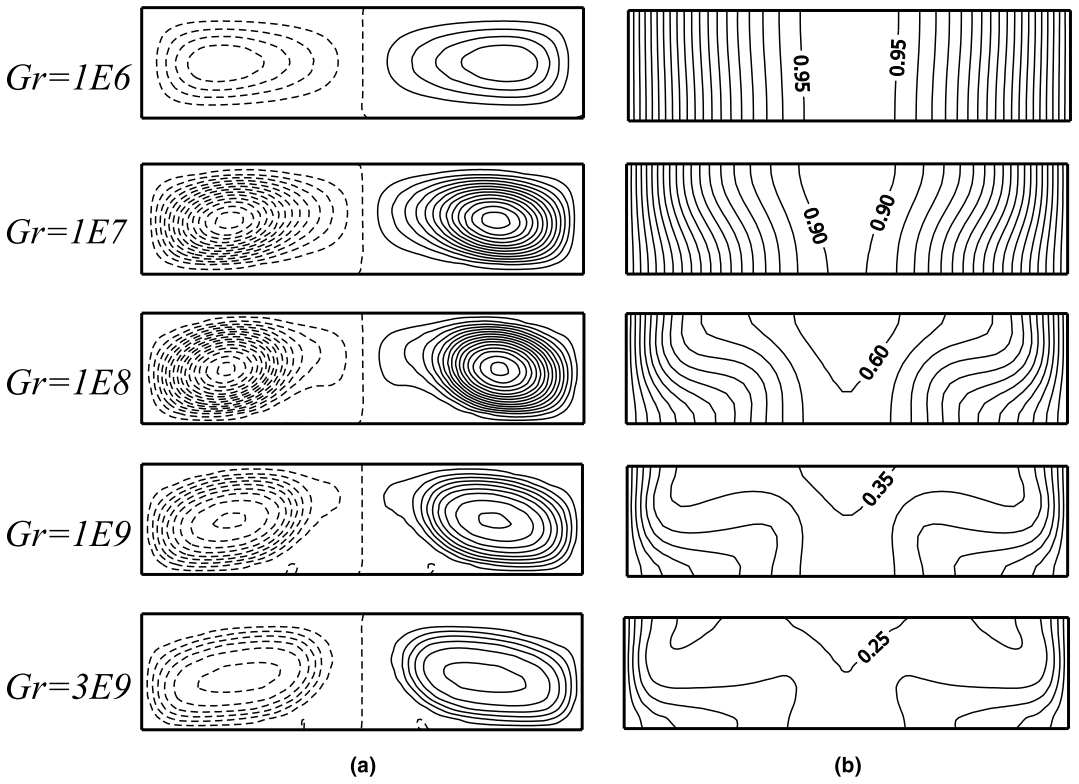

Fig. 4. Flow and temperature fields for all cases attaining symmetric steady-state conditions. (a) Streamlines (dimensionless interval 0.01); solid lines: clockwise flow; broken lines: counter-clockwise flow. (b) Isotherms (dimensionless interval 0.05).

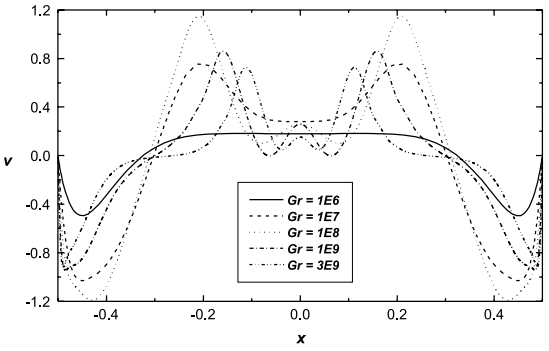

Fig. 5. Profiles of the dimensionless vertical velocity v along the centreline $y = 0$ for the steady-state cases ($Gr = 10^6$ to 3×10^9).

$\sim$1.2 for $Gr = 10^8$ and then decreases again, while the corresponding peaks move toward the centre of the cavity. However, at all Gr, the v velocity is positive (i.e., the flow is directed upward) throughout the central region of the enclosure, and no rotational motion occurs. In the downcoming boundary layers peak negative velocities become largest (~ -1.2) for $Gr = 10^8$, when also the distance of v peaks from the walls is largest ($\sim$0.08 in dimensionless form).

The formation of a quasi-stagnant central region, characterized by low values of the vertical velocity, is peculiar to the present aspect ratio, in which the two main circulation rolls are widely separated, and was not observed for the previously studied values of AR (i.e., 4 and 1). On the whole, the behaviour of v profiles suggests that higher-order harmonics progressively enter the solution as Gr increases. The flow remains bilaterally symmetric at all Gr.

4. Periodic flow

For a Grashof number of 10^{10} a perfectly time-periodic solution was predicted. Fig. 6 reports the time-dependent behaviour of vertical velocity v at points 1 and 4 (a) and of mean and maximum temperatures (b). Following an initial transient quite similar to that reported for the stationary solutions at $Gr = 10^8$ and 10^9 (see Fig. 3), at $t \approx 10$ the flow destabilizes and results in perfectly periodic oscillations at $t \approx 30$. The frequency of the oscillation is $\sim$1.4 in dimensionless form (F_0 units). The oscillations are smoothed for the maximum temperature T_{max} in Fig. 6(b), and are almost completely absent for the spatially averaged temperature $\langle T \rangle$.

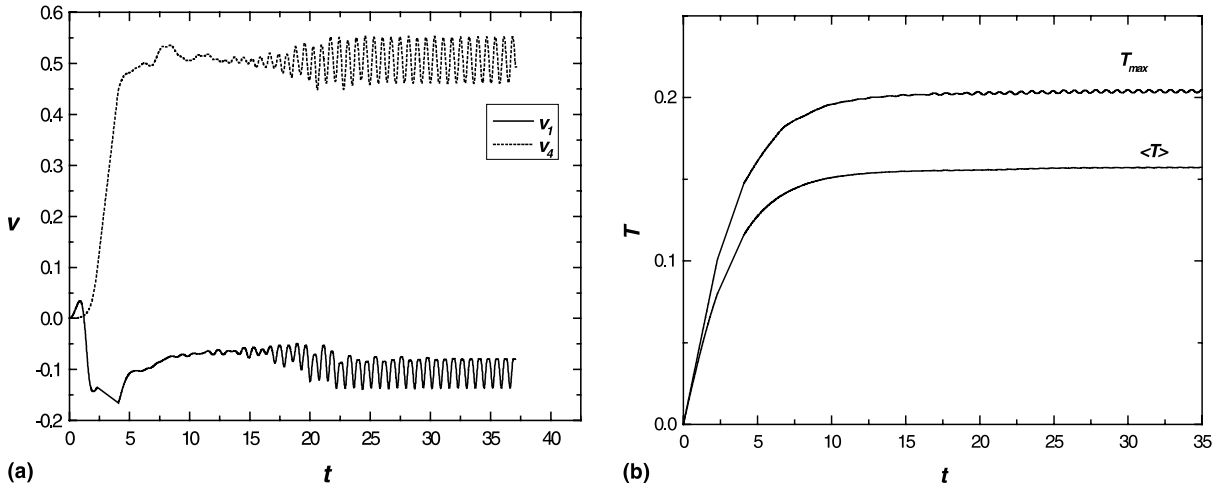

Fig. 6. Results for $Gr = 10^{10}$ (periodic flow). Dimensionless vertical velocity v at monitoring points P1 and P4. Dimensionless mean and maximum temperatures.

The dynamic evolution of the system towards a limit cycle (periodic flow) is evidenced in Fig. 7(a). This reports the vertical velocity v at the monitoring point 5 (located in the upper left region of the enclosure) as a function of the vertical velocity v at point 1 (located in the lower left region of the enclosure, see Fig. 1) during the last stages of the initial transient and the fully developed periodic flow regime. As discussed in [7], such plots can be regarded as simple two-dimensional sections of the trajectory described by the dynamical system in the appropriate, multi-dimensional phase space, and show its relaxation onto the system's attractor (in this case, the limit cycle characteristic of a periodic flow). Similar graphs are reported in Figs. 7(b) and (c) also for higher Grashof numbers, as will be discussed later.

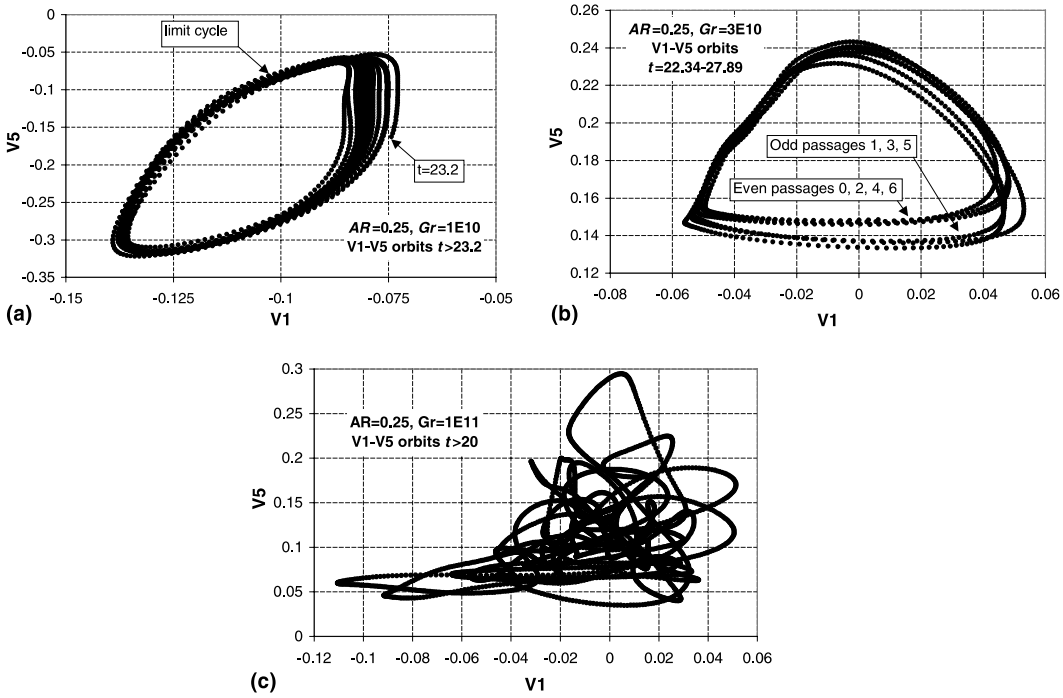

Fig. 7. Plots of vertical velocity at point 5 versus vertical velocity at point 1 (see Fig. 1) for time-dependent cases (see text for details). (a) $Gr = 10^{10}$ (periodic flow); (b) $Gr = 3 \times 10^{10}$ (early chaotic flow); (c) $Gr = 10^{11}$ (fully chaotic flow).

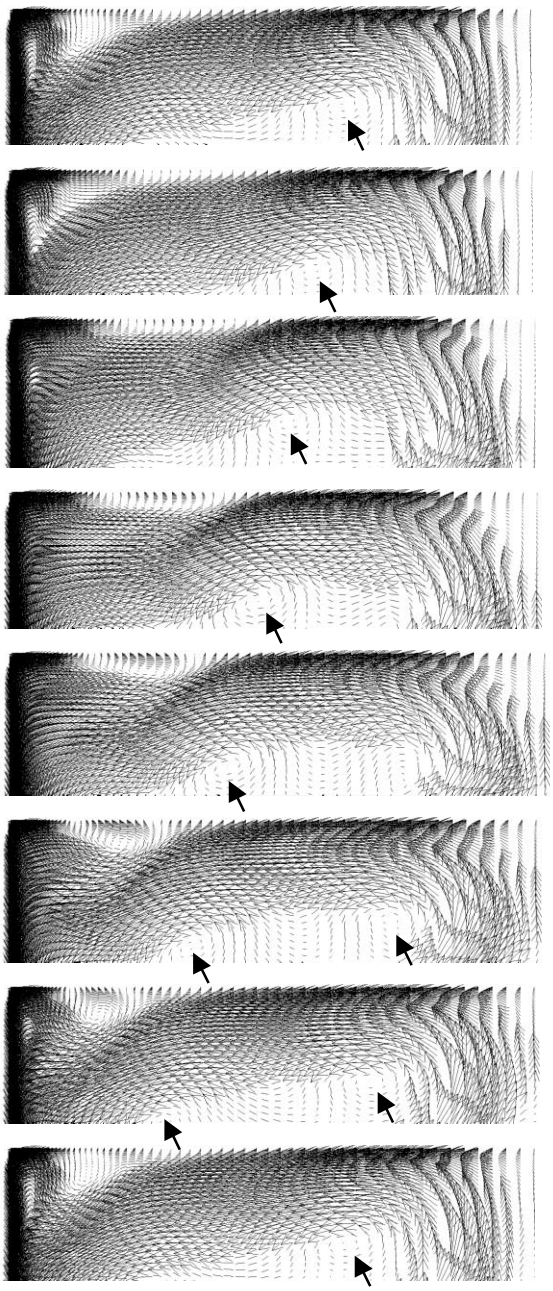

Fig. 8. Time-dependent velocity field for $Gr = 10^{10}$ (periodic flow). Only the upper left quadrant of the enclosure is shown. The (dimensionless) time between consecutive plots is 0.1, and the sequence shown covers ~1 period. Arrows indicate small co-rotating vortices shed downstream along the inner edge of the upper boundary layer.

Some significant features of the periodic time-dependent flow are evidenced in Fig. 8. This reports consecutive velocity vector plots in the upper left quarter of the enclosure; the snapshots are taken after the periodic regime has already been attained and are separated by a dimensionless time interval of ~0.1, so that the sequence covers roughly one period. The flapping of the upper boundary layer can be observed; it is accompanied by the periodic formation of a re-circulation region adjacent to the top wall, which is counter-rotating with respect to the main circulation (i.e., clockwise in this left region of the enclosure). Also the periodic generation of small co-rotating (anti-clockwise) vortices on the inner edge of the upper boundary layer can be observed; these vortices (evidenced by arrows in the figure) are generated near the central rising plume and are shed towards the walls. As previously observed, a perfect bilateral symmetry is maintained at any instant.

This flow picture is qualitatively different from that observed in the periodic regime for AR = 4, characterized by the downward motion of staggered circulation rolls, and for AR = 1, characterized by the small cyclic motion of the two main circulation rolls representing the left–right asymmetric base flow.

Time-sequences of the temperature distribution for the same periodic case $Gr = 10^{10}$ show only few details, since oscillations are smoothed by the high thermal diffusivity of the liquid metal, and have not been reported. Time-averaged flow and temperature fields are reported in Fig. 9 together with results for higher Gr, which will be discussed further on. The perfect bilateral symmetry can be observed. The circulation intensity is lower than that observed for the steady-state case at $Gr = 3 \times 10^9$, see Fig. 4(a), maxima of the (dimensionless) stream function Ψ being ~0.4 against ~0.6. Temperature maxima are slightly lower (0.2 against 0.25). On the whole, however, the time-averaged flow and temperature fields are quite similar to their steady-state counterparts observed at lower Grashof numbers, and follow the same trend.

The time-averaged profile of the vertical velocity v along the midline $y = 0$ is reported in Fig. 10 together with the results obtained for higher Grashof numbers. This profile is similar to those obtained for the steady-state cases, Fig. 5, and follows the same trend; it is characterized by thin descending wall boundary layers and by a bimodal distribution in the central rising plume, with a relative minimum in the centre ($x = 0$). The small central relative maximum observed for the previous, steady-state, cases is now absent while small velocity kinks appear near the edges of the rising plume.

5. Chaotic flow

For $Gr = 3 \times 10^{10}$ and 10^{11} chaotic time-dependent solutions were predicted.

Fig. 11(a) reports the time-dependent behaviour of vertical velocity v at the pairs of monitoring points 1 and 2 and 3–5, symmetrically located with respect to the

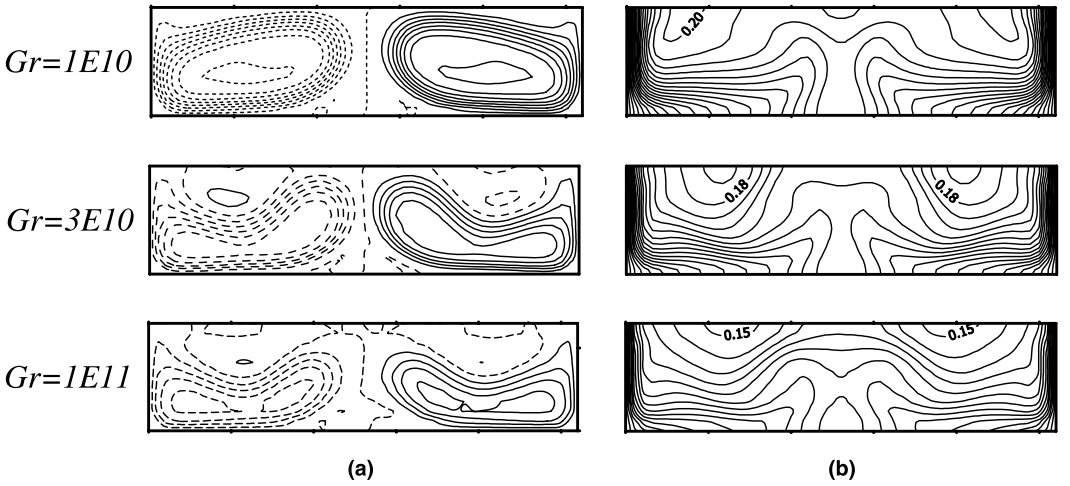

Fig. 9. Time-averaged flow and temperature fields for $Gr = 10^{10}$ (periodic flow), $Gr = 3 \times 10^{10}$ (early chaotic flow), and $Gr = 10^{11}$ (fully chaotic flow). (a) Streamlines (dimensionless interval 0.005); solid lines: clockwise flow; broken lines: counter-clockwise flow. (b) Isotherms (dimensionless interval 0.01).

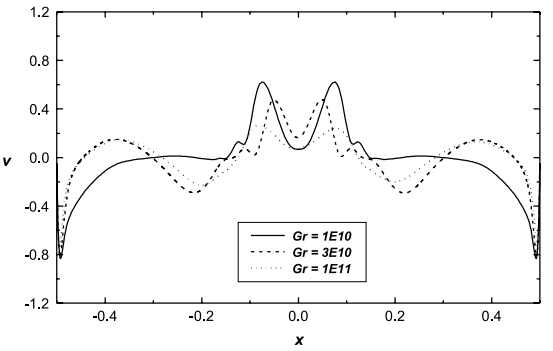

Fig. 10. Profiles of the dimensionless vertical velocity v along the centreline $y = 0$ for the time-dependent cases ($Gr = 10^{10}$ to 10^{11}).

cavity vertical centreline, for $Gr = 3 \times 10^{10}$. It can be observed that, following an initial transient ($t > 10$ to 15), up to $t \approx 28$ velocities at symmetric points oscillate in an almost periodic fashion and remain strictly identical, as in the previous periodic case $Gr = 10^{10}$. However, at $t \approx 28$ velocities like v_3 and v_5 begin to diverge until, at $t \approx 40$, all phase correlations among them are lost and a chaotic flow is obtained. The following oscillations are larger in the upper part of the cavity (points 3–5) than in the bottom region (points 1 and 2).

The mechanism of transition from almost periodic to chaotic flow can be appreciated also by considering Fig. 7(b). Here the trajectory of the system in the plane v_1–v_5 is plotted for the short time interval between $t = 22.34$ and $t = 27.89$ (dimensionless), encompassing about six periods of oscillation (0.925). The shape of the

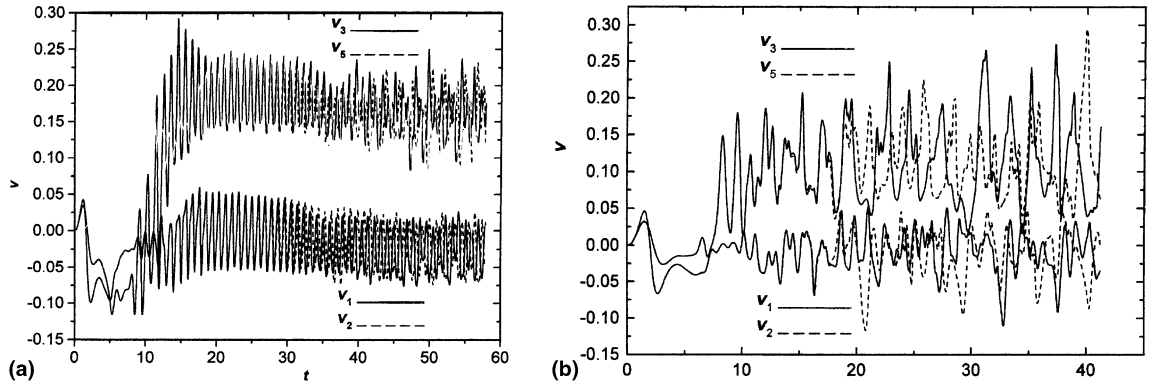

Fig. 11. Time-dependent behaviour of the dimensionless vertical velocity v at monitoring points P1–P2 and P3–P5, showing symmetry breaking and transition to chaotic flow. (a) $Gr = 3 \times 10^{10}$ (early chaotic flow); (b) $Gr = 10^{11}$ (fully chaotic flow).

trajectories suggests that a *period doubling* mechanism is involved in the breakdown of the periodic flow and in the consequent evolution to chaotic motion.

Time series of the vertical velocity v at monitoring points 1 and 2 and 3–5 for $Gr = 10^{11}$ are reported in Fig. 11(b). In this case, following a transient of about 10 τ_0 units, irregular oscillations develop, which, however, maintain the bilateral symmetry up to $t \approx 15$. Only for larger dimensionless times the symmetry is broken and the time series relative to spatially symmetric points become totally uncorrelated. Oscillations are broader than in the previous case at $Gr = 3 \times 10^{10}$, and remain larger in the upper region of the cavity.

A time sequence of the flow field for $Gr = 10^{11}$ is shown in Fig. 12(a), which reports maps of the stream function. The dimensionless time interval between frames is ~0.2. In the instantaneous field the bilateral symmetry is almost completely lost and chaotic flow is clearly indicated by the irregular shape of the streamlines. The top-wall boundary layers which originate from the central rising plume separate after a short distance from the centreline and re-attach on the top wall close to the vertical side boundaries, thus determining counter-rotating recirculation regions of the quasi-stagnant fluid adjacent to the top wall. The early separation of the top-wall boundary layers is probably due to a "rebound" effect following the high-speed impact of the rising plume against the upper wall. The stagnation regions attached to the top wall are also associated with temperature maxima, as clearly shown by the corresponding time sequence of the temperature field in Fig. 12(b).

Time-averaged fields for the two chaotic cases $Gr = 3 \times 10^{10}$ and $Gr = 10^{11}$ are shown in Fig. 9; the left–right bilateral symmetry is clearly recovered both in the flow field and in the temperature distribution. Maxima of T near the top wall are still marked in the time-averaged results, showing that recirculation regions are stable features of the flow at all times.

Time-averaged profiles of the vertical velocity v along the midline $y = 0$ for the same two chaotic cases are reported in Fig. 10. With respect to the profiles observed for the steady-state and periodic cases, they exhibit regions of positive v velocity for $x \approx \pm 0.4$ and negative v velocity for $x \approx \pm 0.2$; these features reflect the shape of the circulation streamlines as plotted in Fig. 9. The central rising plume remains characterized by symmetric velocity maxima on the two sides of a central minimum.

6. Wall shear stress and heat transfer

Fig. 13 reports profiles of the wall shear stress S_w, normalized by $\mu U_0/D$, along the horizontal and vertical

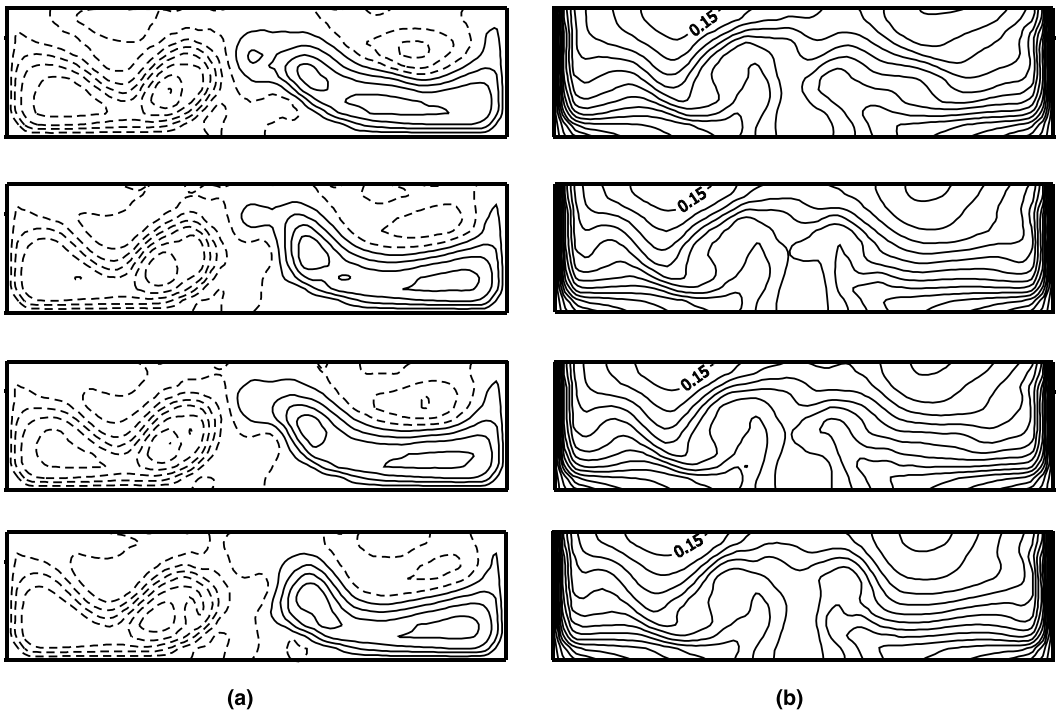

Fig. 12. Time-dependent flow and temperature fields for $Gr = 10^{11}$ (fully chaotic flow). The (dimensionless) time interval between frames is 0.2. (a) Streamlines (dimensionless interval 0.005); solid lines: clockwise flow; broken lines: counter-clockwise flow. (b) Isotherms (dimensionless interval 0.01).

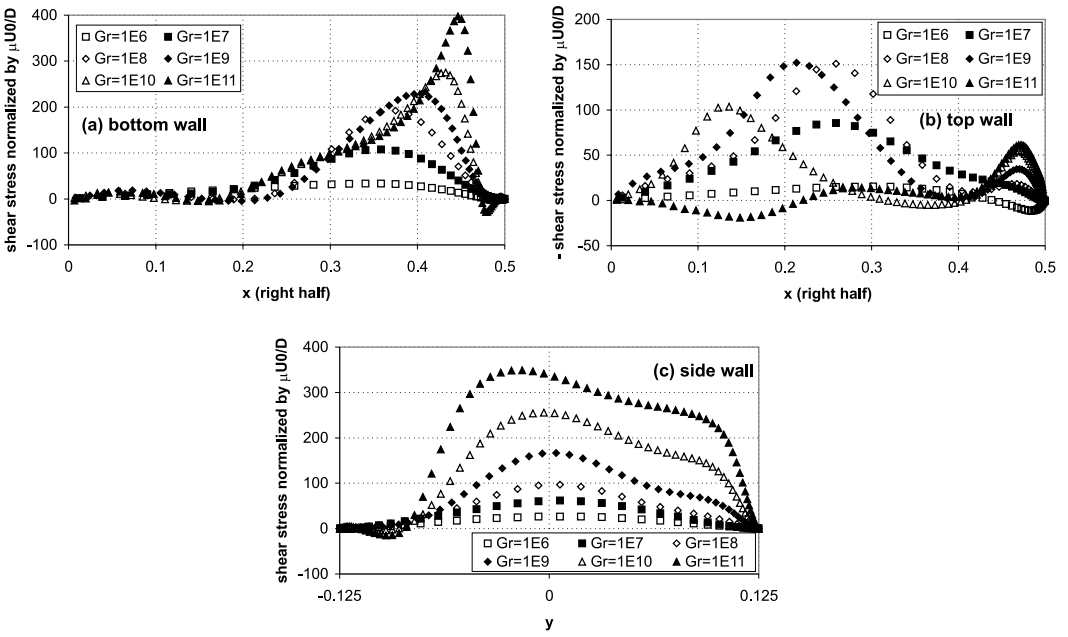

Fig. 13. Profiles of the wall shear stress along the walls for different values of the Grashof number. S_w is normalized by $\mu U_0/D$. For time-dependent cases, time averages are shown. (a) bottom wall; (b) top wall; (c) side walls (left–right average).

(thermally active) walls for different values of the Grashof number. For time-dependent cases, time averages are shown. Due to the bilaterally symmetric nature of the flow, only profiles relative to the right half of the enclosure are reported.

The behaviour of S_w along the *vertical* side walls, Fig. 13(c), is fairly simple. At low *Gr*, profiles are rather flat; at higher *Gr* ($\geqslant 10^9$), a flat peak is associated with the impingement of the flow on the cold side wall, and a small region of negative values, corresponding to a counter-rotating recirculation cell, can be observed near the bottom corner. S_w levels increase monotonically with increasing *Gr*. This behaviour is substantially different from that observed for the previous aspect ratios 4 and 1 [7,8], where a marked peak of wall shear stress was associated with the impingement of hot fluid on the vertical wall.

Profiles of S_w along the *horizontal* walls are more complex. A considerable asymmetry exists between the top and bottom walls at all Grashof numbers. For the periodic and chaotic cases ($Gr = 10^{10}$ and 10^{11}) the bottom wall profiles, Fig. 13(a), exhibit a sharp peak near the corner and flat, low values elsewhere; the top wall profiles, Fig. 13(b), show ample regions of negative stress, associated with the separated-flow regions visible in the stream function maps of Fig. 9(a). Levels of S_w do not vary monotonically with *Gr*; on the top wall, in particular, the highest values are attained at $Gr \approx 10^8$ to 10^9.

Fig. 14 reports the values of S_w averaged along the walls as functions of *Gr* in the whole range investigated.

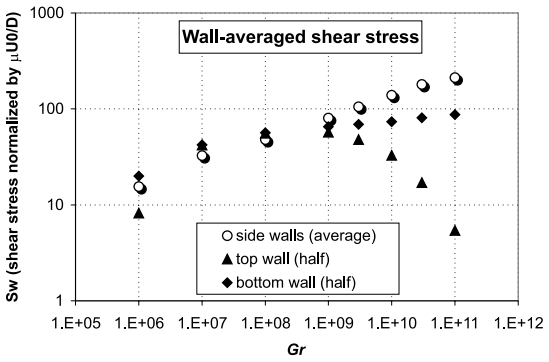

Fig. 14. Wall shear stress, averaged along the top, bottom and side walls and normalized by $\mu U_0/D$, as a function of *Gr*. For time-dependent cases, time averages are shown.

The mean value along the *vertical* side walls increases monotonically with *Gr* following roughly a 0.25 power law. If, following previous work [7,8], the mean side-wall shear stress is normalized by the *hydraulic* scale ρU_0^2 rather than by the *viscous* scale $\mu U_0/D$, i.e., is expressed as a friction coefficient, then it decreases roughly as $Gr^{-0.25}$, less steeply than that observed for AR = 4 and 1 ($\sim Gr^{-1/3}$), and attains much lower values, e.g. $\sim$0.3 against $\sim$2.6 (AR = 4) and $\sim$1.7 (AR = 1) in the limit of low *Gr*.

The mean values for the horizontal walls, also reported in Fig. 14, were computed for the right half of the

cavity only and represent the stress exerted by the wall on the fluid in the direction opposite to that of the main circulation (i.e., $-x$ for the top wall and $+x$ for the bottom wall). Of course, the mean values along the whole top or bottom wall would vanish due to the symmetric nature of the flow (at least in the time averages). The mean S_w computed along the *bottom* wall increases monotonically with Gr like that computed along the side wall, but less rapidly. That computed along the *top* wall attains a maximum at $Gr = 10^8 \sim 10^9$, as commented above in discussing the corresponding profiles, and decreases at higher Gr (corresponding to time-dependent flow) due to the influence of the large recirculation regions adjacent to the upper boundary of the enclosure.

Fig. 15 reports profiles of the wall heat flux q'' for all cases investigated; time averages are shown in the case of time-dependent solutions. Values are normalized by the mean heat flux $qD/2$.

The trend exhibited by the q'' distributions is similar to that discussed for higher values of AR [7,8]; profiles

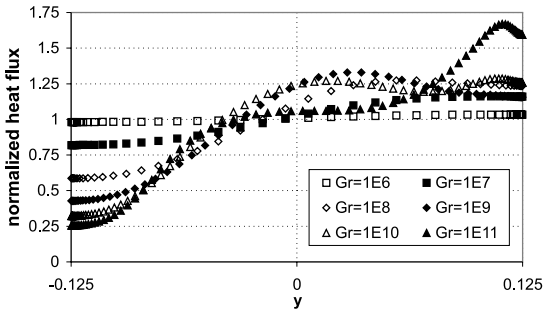

Fig. 15. Profiles of the wall heat flux q'' along the vertical walls for different values of the Grashof number. q'' is normalized by its mean value $qD/2$. For time-dependent cases, time averages are shown.

are rather flat at the lowest Grashof numbers, when convection is negligible, while a larger non-uniformity occurs at higher Gr. Peak values ($\sim$1.7) are obtained for the chaotic flow case at $Gr = 10^{11}$ in the upper corner regions, where the hot fluid advected by the upper horizontal boundary layers meets the cold vertical walls. As in the case AR $= 1$, and unlike in the case AR $= 4$, no uniform-q'' region is observed near the midplane $y = 0$.

The two Nusselt numbers Nu_1 and Nu_2 are reported as functions of the Grashof number in Fig. 16. For comparison purposes, this includes also the results obtained in the previous work for AR $= 4$ and 1.

For the present AR, the first Nusselt number, based on maximum temperature, attains values around 1 (pure conduction) for the lower Grashof numbers ($Gr = 10^6$, 10^7); unlike in the AR $= 4$ and 1 cases, values of Nu_1 below 1 are *not* observed. The transition to chaotic flow at $Gr = 1 \sim 3 \times 10^{10}$ is clearly associated with a reduction in the rate of increase of Nu_1. The second Nusselt number, obtained from the average temperature, increases more regularly and follows roughly a power law $Nu_2 = \text{constant}\, Gr^{1/5}$ in the range $Gr \geqslant 10^7$; this slope is slightly higher than that obtained for the previous AR values of 4 and 1 ($\sim$1/7 and $\sim$1/6, respectively). Significant convective heat transfer ($Nu_1 \approx 3.74$, $Nu_2 \approx 3.32$) is obtained for $Gr = 3 \times 10^9$, still within the steady-state range.

As a first remark, the Nu versus Gr dependence appears to be much similar for all values of AR, showing that Gr (based on cavity width) accounts for most of the variations in Nu while the independent influence of AR is but marginal. The discrepancy observed at intermediate values of Gr ($10^7 \sim 10^8$) is mainly due to the different values of Gr at which transitions between flow regimes occur in enclosures with different AR, see below.

It should be observed that the relation $Nu = \text{constant}\, Gr^{1/5}$, taking account of the definition of the Grashof number as proportional to D^5, simply expresses

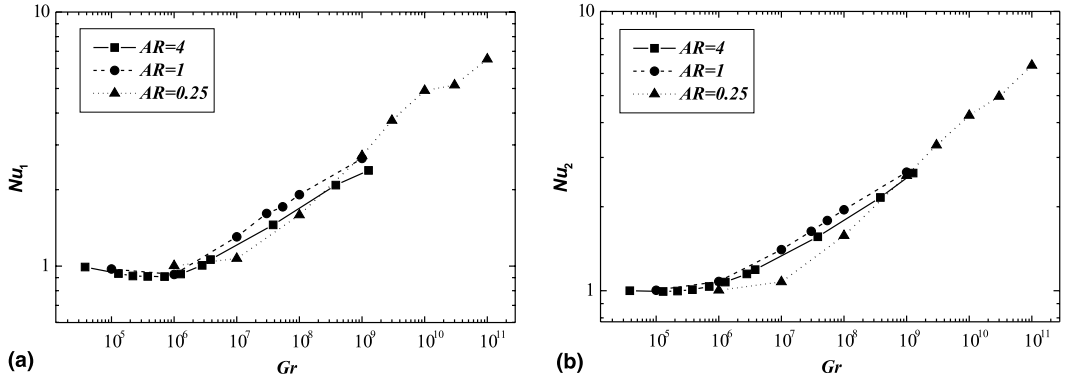

Fig. 16. Behaviours of the Nusselt numbers $Nu_1 = 1/T_{max}$ (a) and $Nu_2 = (2/3)/\langle T \rangle$ (b) as functions of the Grashof number for AR $= 4$, 1, and 0.25.

the fact that $Nu = \text{constant}\,D$, i.e., that the heat transfer coefficient $h = Nuk/D$ does *not* depend upon the enclosure lateral size D, as expected in the separated-boundary layer regime in any confined free convection problem (for example, the same 1/5-power dependence is reported [1] for a similar configuration but higher Pr). Similar remarks hold for the $Nu = \text{constant}\,Gr^{1/3}$ dependence in the case of *differentially* heated enclosures. Curiously, not all authors highlight this simple meaning of the power-law Nu–Gr relationships as it deserves.

7. Influence of the aspect ratio on flow stability

As discussed above, heat transfer depends mainly on the Grashof number Gr based on the cavity width D, and only marginally on the aspect ratio. On the other hand, an overall comparison of the present findings for $\mathrm{AR} = 0.25$ with previous results for $\mathrm{AR} = 4$ and 1 [7,8] shows that the transitions to time-dependent and chaotic flow occur at broadly different values of Gr, indicating a strong influence of the aspect ratio. Fig. 17 reports the (approximate) critical Grashof number for transition from steady-state to periodic flow as a function of AR. The asymptotic linear stability results for an infinitely slender enclosure [1] and the present Prandtl number of 0.0321 are also included. It can be observed that the results for $\mathrm{AR} = 4$, 1, and 0.25 are roughly aligned in a doubly logarithmic graph and follow an $\mathrm{AR}^{-3.5}$ power law. The value obtained for $\mathrm{AR} = 4$ ($Gr \sim 2.8 \times 10^5$) is close to that ($\sim 10^5$) deduced from the linear stability analysis in [1]. No comparable results are available in the literature for the opposite case of an infinitely shallow enclosure cooled from the sides ($\mathrm{AR} \to 0$, question marks in the graph), but it can be inferred on physical grounds that the critical Grashof number for loss of stability of the base steady-state solution must diverge.

Since, up to $\mathrm{AR} \sim 4$, the marginal stability curve in Fig. 17 exhibits a slope close to −3, it may be concluded

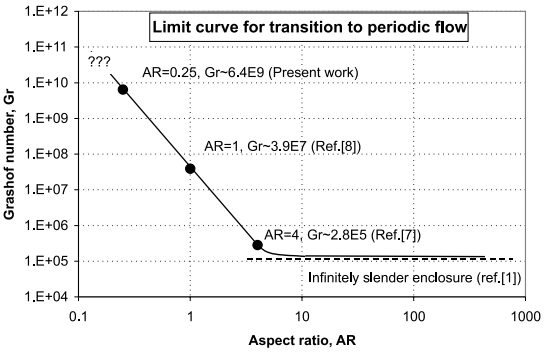

Fig. 17. Limit curve for transition from steady-state to time-dependent flow in the AR–Gr plane.

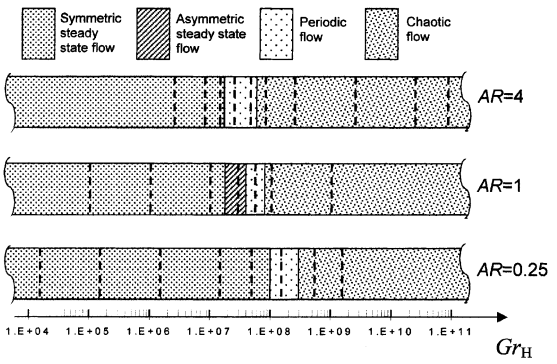

Fig. 18. Summary map of flow regimes for three values of the aspect ratio. The horizontal axis reports $Gr_\mathrm{H} = Gr \times \mathrm{AR}^3$, i.e., the Grashof number based on maximum conductive temperature and cavity *height*.

that *in this range* the transition to time-dependent flow is governed mainly by the Grashof number based on maximum conductive temperature and cavity *height*, $Gr_\mathrm{H} = \mathrm{AR}^3 Gr$, with only a minor residual influence of AR. Fig. 18 reports a schematic flow regime map as a function of Gr_H and AR; dashed lines indicate the test cases for which direct numerical simulations were performed, and different flow regimes (symmetric steady-state, asymmetric steady-state, periodic, and chaotic) are visualized by different shadings. Transition to periodic flow occurs at $Gr_\mathrm{H} \approx 2 \times 10^7$ for $\mathrm{AR} = 4$, $Gr_\mathrm{H} \approx 4 \times 10^7$ for $\mathrm{AR} = 1$ and $Gr_\mathrm{H} \approx 10^8$ for $\mathrm{AR} = 0.25$. Transition to chaotic motion occurs at $Gr_\mathrm{H} \approx 6 \times 10^7$ for $\mathrm{AR} = 4$, $Gr_\mathrm{H} \approx 10^8$ for $\mathrm{AR} = 1$ and $Gr_\mathrm{H} \approx 3 \times 10^8$ for $\mathrm{AR} = 0.25$. The transition from symmetric to asymmetric steady states occurs at $Gr_\mathrm{H} \approx 2 \times 10^7$ only for $\mathrm{AR} = 1$ and does *not* occur at other aspect ratios. A further transition [8], predicted for the square enclosure only (i.e., that from chaotic flow with asymmetric time averages to chaotic flow with symmetric time averages), is not reported for the sake of simplicity.

However, from the asymptotic behaviour in Fig. 17 it is clear that the dependency of transitions upon Gr_H is *not* a universal feature of the flow and cannot be extended to high values of the aspect ratio ($\mathrm{AR} > 4$).

8. Conclusions

Numerical simulations were conducted for an internally heated rectangular enclosure at $\mathrm{AR} = 0.25$ and Gr ranging from 10^6 to 10^{11}. The Prandtl number was 0.0321. A sequence of different flow regimes from steady laminar to periodic and chaotic was clearly identified.

In this shallow cavity, transition from steady to periodic flow occurred at a relatively high Gr (3×10^9–10^{10}) and resulted in a regular flapping motion of

the horizontal top-wall boundary layers, in the outward travelling-wave motion of flow disturbances (secondary rolls) along their inner edges, and in a pulsatile behaviour of the flow rate in the central rising plume. The periodic flow was bilaterally symmetric at all instants.

Chaotic flow was predicted at $Gr \geqslant 3 \times 10^{10}$; while the general features of the secondary flow were similar to those observed for the periodic case, flow oscillations were now irregular and instantaneously asymmetric in the left and right halves of the cavity. Transition to chaotic flow appeared to be associated with a loss of stability of the central rising plume, which started to oscillate thus breaking the instantaneous symmetry of the flow field. However, long-term time averages maintained bilateral symmetry.

The present paper concludes our study on low-Prandtl number free convection in two-dimensional, internally heated rectangular enclosures. Future work will address the influence of Prandtl number, three-dimensionality, and additional body forces such as produced by magnetohydrodynamic interactions.

References

[1] F.A. Kulacki, D.E. Richards, Natural convection in plane layers and cavities with volumetric energy sources, in: S. Kakaç, W. Aung, R. Viskanta (Eds.), Natural Convection – Fundamentals and Applications, Hemisphere, New York, 1985, pp. 179–254.

[2] B. Farouk, Turbulent thermal convection in an enclosure with internal heat generation, ASME J. Heat Transfer 110 (1988) 126–132.

[3] H. Fiedler, R. Wille, Wärmetransport bie frier Konvektion in einer horizontalen Flussigkeitsschicht mit Volumenheizung, Teil 1: Integraler Wärmetransport, Rep. Dtsch Forschungs-Varsuchsanstalt Luft-Raumfahrt, Inst. Turbulenzfenschung, Berlin, 1971.

[4] F.A. Kulacki, M.E. Nagle, Natural convection in a horizontal fluid layer with volumetric energy sources, ASME J. Heat Transfer 91 (1975) 204–211.

[5] P.G. Daniels, O.K. Jones, Convection in a shallow rectangular cavity due to internal heat generation, Int. J. Heat Mass Transfer 41 (1998) 3979–3987.

[6] E. Proust, L. Anzidei, G. Casini, M. Dalle Donne, L. Giancarli, S. Malang, Breeding blanket for DEMO, Fusion Eng. Des. 22 (1993) 19–33.

[7] I. Di Piazza, M. Ciofalo, Low-Prandtl number natural convection in volumetrically heated rectangular enclosures I. Slender cavity, $AR = 4$, Int. J. Heat Mass Transfer 43 (2000) 3027–3051.

[8] S. Arcidiacono, I. Di Piazza, M. Ciofalo, Low-Prandtl number natural convection in volumetrically heated rectangular enclosures II. Square cavity, $AR = 1$, Int. J. Heat Mass Transfer 44 (2001) 537–550.

[9] M. Lésieur, Turbulence in Fluids, Kluwer Academic Publishers, Amsterdam, 1990.

[10] J.R. Van Doormal, G.D. Raithby, Enhancements of the SIMPLE method for predicting incompressible flows, Numer. Heat Transfer 7 (1984) 147–163.

[11] CFX 4.1 flow solver user guide, Computational Fluid Dynamics Services, AEA Technology, Harwell Laboratories, UK, 1995.